Core-shell nanostructure in a $Ge_{0.9}Mn_{0.1}$ film from structural and magnetic measurements

P. Dalmas de Réotier,[1,2] E. Prestat,[3,4] P. Bayle-Guillemaud,[3,4] A. Barski,[3,4] A. Marty,[3,4] M. Jamet,[3,4] A. Suter,[5] T. Prokscha,[5] Z. Salman,[5] E. Morenzoni,[5] and A. Yaouanc[1,2]

[1] *Univ. Grenoble Alpes, INAC-SPSMS, F-38000 Grenoble, France*
[2] *CEA, INAC-SPSMS, F-38000 Grenoble, France*
[3] *Univ. Grenoble Alpes, INAC-SP2M, F-38000 Grenoble, France*
[4] *CEA, INAC-SP2M, F-38000 Grenoble, France*
[5] *Laboratory for Muon-Spin Spectroscopy, Paul Scherrer Institute, CH-5232 Villigen-PSI, Switzerland*

(Dated: May 19, 2014)

We have characterized a film of $Ge_{0.9}Mn_{0.1}$ forming self-organized nanocolumns perpendicular to the Ge substrate with high resolution scanning transmission electron microscopy combined with electron energy loss spectroscopy, and bulk magnetization and positive muon spin rotation and relaxation (μSR) measurements. The Mn-rich nanocolumns form a triangular lattice with no detectable Mn atoms in the matrix. They consist of cores surrounded by shells. The combined analysis of bulk magnetization and μSR data enables us to characterize the electronic and magnetic properties of both the cores and shells. The discovered phase separation of the columns between a core and a shell is probably relevant for other transition-metal doped semiconductors.

arXiv:1405.4238v1 [cond-mat.mes-hall] 16 May 2014

Spin-polarized carriers in spintronic applications may be conveyed by conventional metallic ferromagnets or by so-called ferromagnetic semiconductors. Until now semiconductor spintronics has mainly been based on diluted magnetic semiconductors [1]. Another route consists in the use of films with a well-defined pattern of transition metal-rich nanostructures with a relatively high-temperature ferromagnetic phase [2–4]. Nanocolumns as in $Ge_{1-x}Mn_x$ films [5, 6] are one of these structures.

The magnetic properties of these films have so far been investigated by x-ray magnetic circular dichroism [7, 8] and electron spin resonance [9, 10], but the most conclusive results stem from superconducting quantum interference device (SQUID) magnetometry [11, 12]. Here we resolve the structure and characterize the magnetism of the nanocolumns of a $Ge_{0.9}Mn_{0.1}$ film at the atomic scale using high resolution scanning transmission electron microscopy (STEM) supplemented with electron energy loss spectroscopy (EELS) analysis, and SQUID and muon spin rotation and relaxation (μSR) measurements. We find the film to consist of nanocolumns embedded in a Ge matrix with less than 0.05 at. % of Mn. Each nanocolumn is made of a core surrounded by a shell with notable different magnetic properties. We suggest that this three-fold structural and magnetic phase separation is generic to impurity doped semiconductors with spinodal decomposition.

Our 80 nm-thick $Ge_{0.9}Mn_{0.1}$ film has been grown by molecular beam epitaxy at low temperature. Ge and Mn atoms have been co-evaporated at 100°C on a Ge(100) substrate using standard Knudsen cells. Due to the very low solubility of Mn in Ge, a spontaneous two-dimensional spinodal decomposition takes place within the film at the early stage of the growth [13]. The following layer-by-layer growth leads to the formation of Mn-rich nanocolumns spanning the whole film thickness [5]. Their average diameter is $d_{\rm nc} = 4$ nm — see the images in the supplemental material [14]. The nanocolumns form a slightly disordered triangular lattice with an average lattice parameter $a_{\rm nc}^{\rm lp} = 10$ nm.

The STEM-EELS analysis was performed at room temperature with an ångström-sized electron probe [14]. The μSR spectra were recorded from 300 down to 5 K at the low energy muon (LEM) spectrometer [14–16] of the Swiss Muon Source (SμS, Paul Scherrer Institute, Switzerland) with a 9 cm^2 area sample. The spectra were taken either in zero or in a finite external field $\mathbf{B}_{\rm ext}$ applied perpendicular to the film substrate.

Results of STEM-EELS measurements are presented in Fig. 1. As shown in Fig. 1b, the nanocolumns exhibit a rather complex inner crystal structure and are surrounded by a Ge matrix with huge tensile strain up to 1.0 (3)%. The Mn content within the nanocolumns is not uniform. As shown in Fig. 1c, they exhibit a core-shell structure with a $d_{\rm c} = 2$ nm core diameter containing up to 70 at. % of Mn surrounded with a $r_{\rm s} = 1$ nm thick shell in which the Mn content decreases roughly linearly from 70 to less than 0.05 at. %, i.e. the detection limit, in the matrix. The average Mn content of 33 at. % over the total area agrees with a previous estimate [17]. Note the nanocolumn core high atomic density: 82 (8) atoms/nm^3 to be compared to 44 atoms/nm^3 in pure Ge. A close packed metallic structure is therefore formed in the nanocolumns. It is tempting to assign it to the most stable Ge-Mn alloy of formula Ge_3Mn_5 since its Mn atomic fraction of 5/8 is close to the value measured in the nanocolumns core [18]. However, x-ray diffraction have definitely excluded the presence of the hexagonal Ge_3Mn_5 phase within the film [19]. Magnetization measurements discussed later on also support this result since the magnetic moment per Mn in the core is much less than 2.6 $\mu_{\rm B}$/Mn in pure Ge_3Mn_5. The

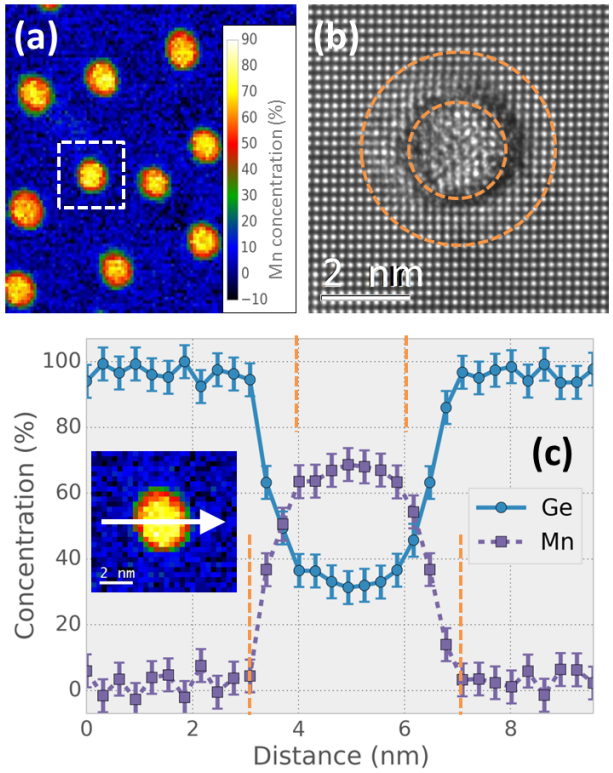

FIG. 1. (Color online) Characterization of our $Ge_{0.9}Mn_{0.1}$ film. (a) Mn concentration map obtained by EELS. (b) STEM plane view. (c) Ge and Mn concentration profiles across a single nanocolumn. In (b) and (c) the orange dashed circles and vertical dashed lines specify the nanocolumn core and shell positions.

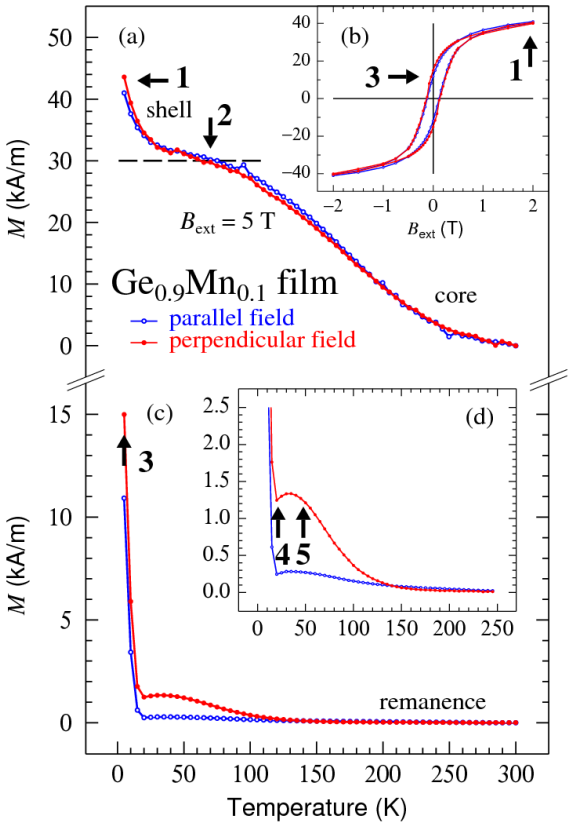

FIG. 2. (Color online) Bulk magnetization measurements for our $Ge_{0.9}Mn_{0.1}$ film normalized to its volume. $\mathbf{B}_{ext}$ is either parallel or perpendicular to the film substrate. (a) Saturation magnetization under 5 T as a function of temperature. (b) Magnetization curves recorded at 5 K. (c) Remanent magnetization as a function of temperature after field cooling under 5 T. For the sake of clarity the magnetization between 5 and 250 K has been enlarged in (d), emphasizing the unexpected uprise of the magnetization above 20 K. The different magnetic configurations denoted 1 to 5 are illustrated in Fig. 3.

Mn atomic density varies from 57 (5) atoms/nm^3 in the nanocolumns core down to approximately zero in the Ge matrix. Assuming a linear Mn concentration profile in the shell, we find that 3/7 (4/7) of Mn atoms are located in the nanocolumns core (shell).

We now discuss our magnetization measurements. With a Mn content less than 0.05%, any magnetic order within the Ge matrix can be ruled out. From Fig. 2a two magnetic transitions are inferred: a first one close to room temperature — to be better defined below by transverse-field (TF)-μSR — at which the nanocolumn cores order, and a second one at ≈ 70 K corresponding to the onset of magnetization in the shell, probably of the spin-glass type owing to the large Mn content change. The respective magnetizations yield the magnetic moment per Mn in both phases: $\mu_{core} = 1.8\ \mu_B$/Mn and an average $\mu_{shell} = 0.6\,\mu_B$/Mn. These values correspond to 827 kA/m and 124 kA/m saturation magnetizations when normalized to the core and shell volumes. The magnetic configurations denoted as 1 to 5 in Fig. 2 are depicted in Fig. 3. Considering their nanometer size, the nanocolumns behave as superparamagnetic nanostructures in SQUID measurements with a maximum blocking temperature $T_B^{SQUID} = 150$ K given by the vanishing remanence in Fig. 2c and the bifurcation between zero field cooling (ZFC) and field cooling (FC) curves in Fig. 4c.

We now analyze our remanence magnetic data in Figs. 2c and d. Because a_{nc}^{lp} is very short an antiferromagnetic order of the nanocolumns should occur through the nanocolumn dipolar coupling [5]. We thus expect no magnetic remanence at low temperature from the nanocolumns cores. In fact, at 5 K we observe quite a large remanent magnetic signal: almost 35% of the saturation magnetic moment. Moreover, it is nearly isotropic and almost disappears at 20 K; see Fig. 2d. This is the

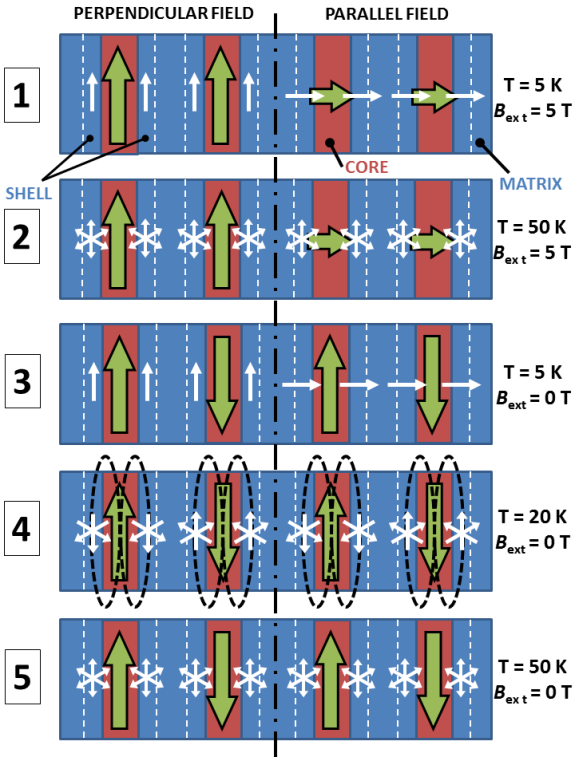

FIG. 3. (Color online) Schematic magnetic configurations for the cores and shells for fields and temperatures defined as labels in Fig. 2. The $\mathbf{B}_{\rm ext}$ direction is relative to the film substrate. **1**: The cores and shells are both ferromagnetically (FM) aligned parallel to $\mathbf{B}_{\rm ext}$: $M^{\rm core} = M_s^{\rm core} \approx 30$ kA/m and $M^{\rm shell} = M_s^{\rm shell} \approx 13$ kA/m where the s subscript denotes the saturation magnetization. **2**: The cores remain FM aligned while the shells become paramagnetic (PM): $M^{\rm core} = M_s^{\rm core}$ and $M^{\rm shell} = 0$. **3**: Remanent state at 5 K after cooling under $B_{\rm ext} = 5$ T. The shell magnetic moments remain in the saturated configuration ($M^{\rm shell} = M_s^{\rm shell}$) whereas the cores contribution plummets because of their basically antiparallel arrangement. Still, when $\mathbf{B}_{\rm ext}$ is perpendicular to the film, some disorder in the columns position yields a small remanent magnetization of about 1.5 kA/m, i.e. $M^{\rm core} \approx M_s^{\rm core}/20$ whereas $M^{\rm core} \approx 0$ for the parallel setup. **4**: The stray field of a core polarizes the PM moments in the shell antiparallel to the core moment: $M^{\rm core} \approx M_s^{\rm core}/20$ and $M^{\rm shell} \propto -M^{\rm core}$ for the perpendicular configuration and $M^{\rm core} = M^{\rm shell} \approx 0$ in the parallel configuration. **5**: The cores remain in a remanent state while the shell moments are no longer polarized by the stray fields: $M^{\rm shell} = 0$ while $M^{\rm core} \approx M_s^{\rm core}/20$ ($M^{\rm core} \approx 0$) in the perpendicular (parallel) configuration.

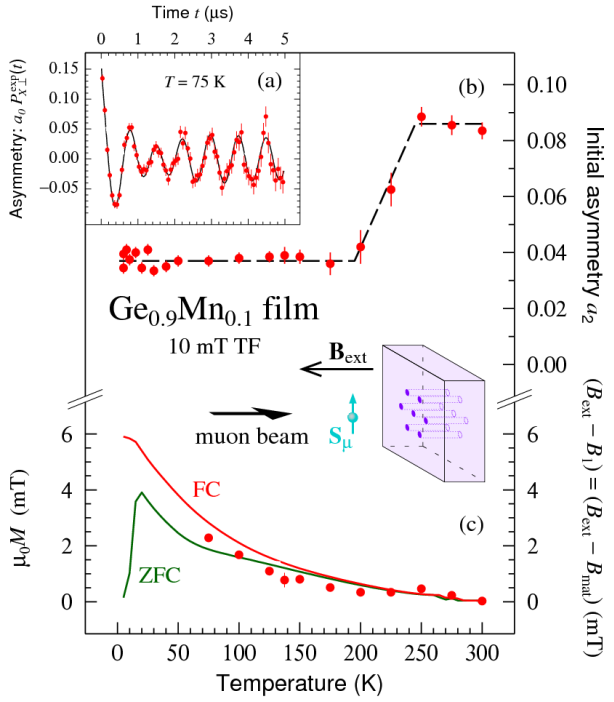

FIG. 4. (Color online) Transverse-field μSR data with $B_{\rm ext} = 10$ mT. (a) A spectrum at 75 K with the result of a fit to Eq. 1. (b) Thermal dependence of the asymmetry a_2, and (c) field difference $(B_{\rm ext} - B_1) = (B_{\rm ext} - B_{\rm mat})$ (bullets) compared to the field $\mu_0 M$, where M is the bulk magnetization measured either with a field or a zero-field cooling procedure (full lines). The TF-μSR geometry is illustrated with the pictogram. The dashed line in panel (b) is a guide to the eyes.

position of the ZFC peak in Fig. 4. Attributing the remanence to the shells, all the results are consistent with a parallel moment alignment in the shell below a critical temperature of 20 K. With this assignment we implicitely assume that there is no exchange magnetic coupling between the cores and shells. The remanent states denoted as 3, 4, and 5 in Figs. 2c and d are explicitely shown in Fig. 3. For $\mathbf{B}_{\rm ext}$ perpendicular to the film substrate, a finite remanent signal is detected above 20 K. We attribute it to disorder within the nanocolumn array which inhibits a perfect cancelation of the core moments. The only coupling between the cores and shells is observed in configuration 4 where the paramagnetic Mn atoms in a given shell are polarized along the stray field from its core leading to a dip in the remanence curve of Fig. 2d.

μSR spectroscopy was used to probe the nanocolumn magnetic state at the atomic scale. In Fig. 4a is shown a typical weak TF-μSR spectrum $a_0 P_{X\perp}^{\rm exp}(t)$ recorded after a FC procedure. $P_{X\perp}^{\rm exp}(t)$ measures the evolution of the muon polarization in a plane perpendicular to $\mathbf{B}_{\rm ext}$ [20]. As explained in Ref. [14], for $40 \le T \le 300$ K

$$a_0 P_{X\perp}^{\rm exp}(t) = a_1 \exp[-(\lambda_{X\perp} t)^{\beta}] \cos(\gamma_\mu B_1 t + \varphi) + a_2 \cos(\gamma_\mu B_{\rm ext} t + \varphi), \quad (1)$$

where φ is a phase constant, $a_1 = 0.13$, and B_1 and a_2 are free parameters. The stretched exponential accounts for the magnetic inhomogeneity and dynamics of the first component. The exponent β has been set in consistency

with zero-field (ZF) data [14]. The relaxation rate $\lambda_{X\perp}$ is so large below 40 K that it cannot be determined with confidence. Still the second component can be analyzed after dropping the initial channels and setting $a_1 = 0$ in Eq. 1. The temperature dependences of a_2 and the field difference $(B_{\rm ext} - B_1)$ are displayed in Fig. 4.

Let us discuss the first component parameters. The matrix between the columns occupying a volume bigger than that of the columns, it is natural to set $a_1 = a_{\rm mat}$, where $a_{\rm mat}$ is the amplitude for the muons implanted in the matrix. As a consequence, $B_1 = B_{\rm mat}$. From Fig. 4c the field difference $B_{\rm mat} - B_{\rm ext}$ is on the order of $-\mu_0 M$. The sign of this field can be understood as follows. In the absence of Mn atoms in the matrix, it is essentially the dipolar field produced by the nanocolumns and is therefore antiparallel to the column moments. We speculate the slight reduction in absolute value of the measured field compared to $-\mu_0 M$ below 200 K (see Fig. 4c) to arise from Mn moments in the shell which are slightly polarized antiparallel to the cores.

We now deal with $a_2(T)$. As the film is cooled below 250 K, a_2 starts to decrease: the nanocolumns enter a magnetic ordered state. The transition is completed at ≈ 200 K at which $a_2(T)$ reaches a plateau. Therefore the transition width is ≈ 50 K with an average ordering temperature $T_c^{\rm core} = 225$ K [21]. In a weak TF-μSR experiment the muons probing a magnetically ordered region — here the columns cores — and its vicinity are rapidly depolarized [22] and do not contribute to the signal. Therefore, we attribute the second component below 200 K to muons implanted in the sample surroundings, i.e. the so-called background with $a_{\rm bg} \simeq 0.035$, a reasonable value. Above $T_c^{\rm core}$, the amplitude $a_{\rm c} = a_2 - a_{\rm bg} \simeq 0.05$, corresponds to muons in the paramagnetic cores and their surroundings [23].

The spin dynamics in our film has been investigated by ZF-μSR measurements. A selection of $a_0 P^{\rm exp}_{Z\,\parallel,\perp}(t)$ spectra with the initial muon polarization $\mathbf{S}_\mu$ either parallel or perpendicular to the film substrate is shown in Fig. 5. $P^{\rm exp}_{Z\,\parallel,\perp}(t)$ denotes the evolution of the projection of the muon polarization along $\mathbf{S}_\mu$. We note three qualitative characteristics. (i) Given the uniaxial character of the nanocolumns, the similitude of the spectra for the two geometries is striking. Since we probe the dynamics of the Mn spins, we conclude that we are dealing with isotropic spins, consistent with a Mn^{2+} electronic state. (ii) The transition from the paramagnetic to the superparamagnetic states is fingerprinted by comparing the spectra at 300 and 200 K. (iii) While the spectral shape monotically evolves as the sample is cooled down to 25 K, the relaxation decreases between 25 and 5 K. A quantitative analysis is given in [14]. The spin-lattice relaxation rate in the matrix $\lambda_{Z\,\parallel\,\rm mat}$ is proportional to the fluctuation time τ of the Mn spins in the shells. From the time window of the μSR technique [20], an upper bound for τ is in

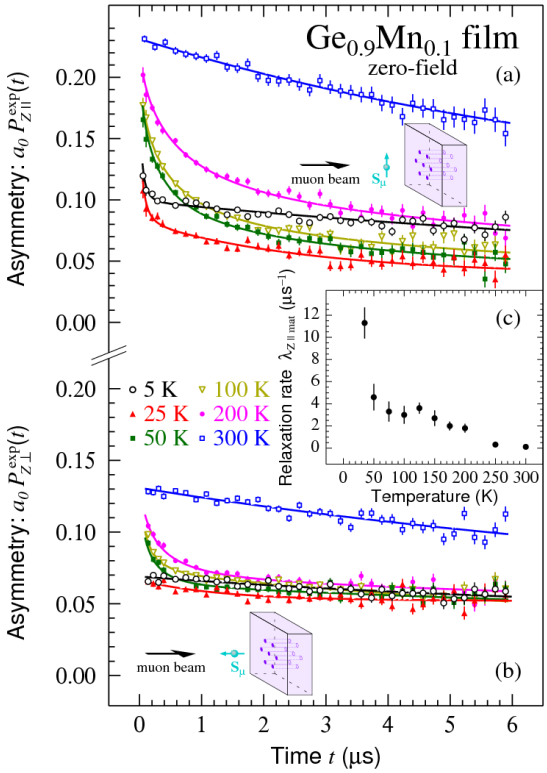

FIG. 5. (Color online) A selection of ZF-μSR spectra for our $Ge_{0.9}Mn_{0.1}$ film with $\mathbf{S}_\mu$ either parallel (panel a) or perpendicular (panel b) to the film substrate. The solid lines arise from fits. The thermal dependence of the μSR spin-lattice relaxation rate $\lambda_{Z\,\parallel\,\rm mat}$ is displayed in panel (c).

the microsecond range. A sharp increase of τ is observed below 50 K (Fig. 5). This is consistent with the remanent magnetization which shows the Mn spins to relax on the SQUID time scale, i.e. on the order of a minute at ≈ 20 K and to be completely frozen at 5 K.

In conclusion, our $Ge_{0.9}Mn_{0.1}$ film of self-organized nanocolumns is a complex object. The columns comprise a core of diameter 2 nm with a nearly 70% Mn atomic concentration, and a shell of thickness 1 nm in which the Mn concentration decreases to 0. The Mn concentration in the matrix between the columns is below the detection limit of 0.05%. A transition from a paramagnetic to a superparamagnetic state is observed for the cores around 225 K. Below 150 K they start to freeze on the SQUID time scale. No magnetic order is found for the Mn moments of the shells. Their spin dynamics is rather isotropic, consistently with a Mn^{2+} state. The shell magnetic moments start to slow down on the microsecond time scale below 50 K and become frozen at 5 K . There is no magnetic coupling between a core and its shell, except for a weak dipolar coupling. Finally we infer that

the separation in three distinct structural and magnetic regions observed here is generic to semiconductors doped with a non miscible transition element.

Part of this work has been performed at the Swiss Muon Source (SμS), Paul Scherrer Institute, Villigen, Switzerland. We thank J.-F. Jacquot for his help during the SQUID measurements.

[1] C. Timm, J. Phys.: Condens. Matter, **15**, R1865 (2003).
[2] D. Bougeard *et al.*, Phys. Rev. Lett., **97**, 237202 (2006).
[3] S. Kuroda *et al.*, Nature Mater., **6**, 440 (2007).
[4] A. Bonanni *et al.*, Phys. Rev. Lett., **101**, 135502 (2008).
[5] M. Jamet *et al.*, Nature Mater., **5**, 653 (2006).
[6] A. P. Li *et al.*, Phys. Rev. B, **75**, 201201 (2007).
[7] S. Tardif *et al.*, Appl. Phys. Lett., **97**, 062501 (2010).
[8] S. Tardif *et al.*, J. Magn. Magn. Mater., **354**, 151 (2014).
[9] A. Jain *et al.*, Appl. Phys. Lett., **97**, 202502 (2010).
[10] A. Jain *et al.*, J. Appl. Phys., **109**, 013911 (2011).
[11] T. Devillers *et al.*, Phys. Rev. B, **76**, 205306 (2007).
[12] I.-S. Yu *et al.*, Phys. Rev. B, **82**, 035308 (2010).
[13] T. Fukushima *et al.*, Jpn. J. Appl. Phys., Part 2, **45**, L416 (2006).
[14] See Supplemental Material for additional information on the structural of the $Ge_{0.9}Mn_{0.1}$ film and on the muon spin rotation and relaxation measurements.
[15] E. Morenzoni *et al.*, J. Phys.: Condens. Matter, **16**, S4583 (2004).
[16] T. Prokscha *et al.*, Nucl. Instr. Meth. A, **595**, 317 (2008).
[17] I. Mouton *et al.*, J. Appl. Phys., **112**, 113918 (2012).
[18] M. Rovezzi *et al.*, Appl. Phys. Lett., **92**, 242510 (2008).
[19] S. Tardif *et al.*, Phys. Rev. B, **82**, 104101 (2010).
[20] A. Yaouanc and P. Dalmas de Réotier, *Muon Spin Rotation, Relaxation, and Resonance: Applications to Condensed Matter*, International Series of Monographs on Physiscs 147 (Oxford University Press, Oxford, 2011).
[21] One could conceive the transition from the paramagnetic to superparamagnetic state of the column cores to take place above room temperature and that the blocking temperature corresponding to the TF-μSR technique is around 225 K where $a_2(T)$ drops — while it is around $T_{\rm B}^{\rm SQUID}$ for the the SQUID measurements. Recalling that the characteristic time scale of TF-μSR is $(\gamma_\mu B_{\rm ext})^{-1} \simeq 1$ μs in our case, this interpretation of the data would lead to an unrealistic short attempt time and therefore cannot hold.
[22] G. M. Luke *et al.*, Phys. Rev. Lett., **73**, 1853 (1994).
[23] The film volume fraction corresponding to the column cores and the region within a distance r from them is $\pi(d_{\rm c}/2+r)^2/[\sqrt{3}(a_{\rm nc}^{\rm lp})^2/2]$ which is equal to $a_{\rm c}/(a_{\rm c}+a_{\rm mat})$ provided that $r = 1.8$ nm. Such a r value is in the accepted range; see e.g. [24].
[24] C. Niedermayer *et al.*, Phys. Rev. Lett., **80**, 3843 (1998).

arXiv:1405.4238v1 [cond-mat.mes-hall] 16 May 2014

Supplemental Material: Core-shell nanostructure in a $Ge_{0.9}Mn_{0.1}$ film from structural and magnetic measurements

P. Dalmas de Réotier,[1,2] E. Prestat,[3,4] P. Bayle-Guillemaud,[3,4] A. Barski,[3,4] A. Marty,[3,4] M. Jamet,[3,4] A. Suter,[5] T. Prokscha,[5] Z. Salman,[5] E. Morenzoni,[5] and A. Yaouanc[1,2]

[1] *Univ. Grenoble Alpes, INAC-SPSMS, F-38000 Grenoble, France*
[2] *CEA, INAC-SPSMS, F-38000 Grenoble, France*
[3] *Univ. Grenoble Alpes, INAC-SP2M, F-38000 Grenoble, France*
[4] *CEA, INAC-SP2M, F-38000 Grenoble, France*
[5] *Laboratory for Muon-Spin Spectroscopy, Paul Scherrer Institute, CH-5232 Villigen-PSI, Switzerland*

(Dated: May 19, 2014)

We provide information on the transmission electron microscopy (TEM) and electron energy loss spectrometry (EELS) techniques we have used, and show additional TEM images, maps and profiles obtained from EELS for our $Ge_{0.9}Mn_{0.1}$ film. Complementary information on the muon spin relaxation measurements and their analysis is given.

I. TRANSMISSION ELECTRON MICROSCOPY AND ELECTRON ENERGY LOSS SPECTROMETRY CHARACTERIZATION

Transmission electron microscopy (TEM) measurement were performed using a monochromated and double-corrected 80-300 kV FEI Titan^3 Ultimate microscope working at 200 kV. Taking advantage of the image-side aberration corrector, high resolution TEM (HRTEM) images were acquired close to Gaussian focus, i.e. within a few nanometers away to avoid delocalization effect. To increase the signal-to-noise ratio of the HRTEM measurement, series of about 10 images have been acquired from the same area. After alignement of the image series using a cross-correlation based algorithm, we averaged the images over the series, to obtain an HRTEM image with very good signal-to-noise ratio. TEM images of a $Ge_{0.9}Mn_{0.1}$ film grown at 100°C are shown in Fig. 1

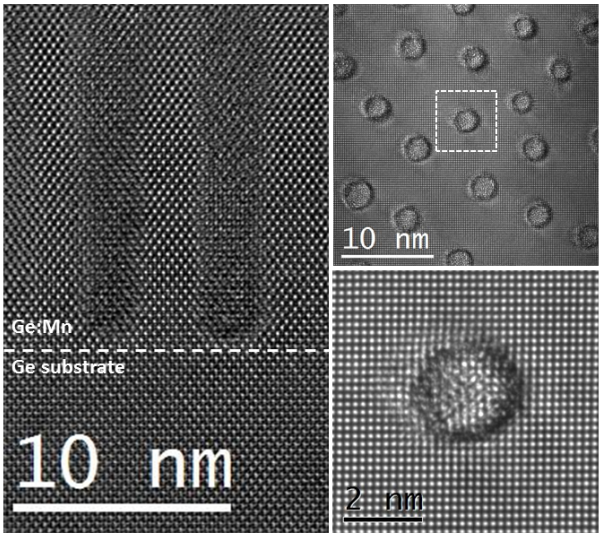

FIG. 1. Low and high resolution TEM images of our $Ge_{0.9}Mn_{0.1}$ film.

Electron energy loss spectroscopy (EELS) acquisitions were achieved using a Gatan imaging filter (GIF) Quantum in dual-EELS mode with an energy dispersion of 1 eV, allowing to acquire a full range electron loss from 0 to 1400 eV. The convergence and collection angles were 20 and 98 mrad, respectively. Typical pixel acquisition time was 20-50 ms and the typical map size was about 200×200 pixels. The pixel size was set to 0.3 nm. The noise of the EELS signal was removed using a principal component analysis (PCA) algorithm implemented in the open-source software Hyperpsy.[1] The relevant number of components for the reconstruction of the spectra was chosen by careful inspection of the factors and loadings of the first 10 components. For each edge (Mn $L_{2,3}$ at 640 eV and Ge $L_{2,3}$ at 1217 eV), the background was removed by subtracting a power law fitted in the region preceding the edge with a width of 40-80 eV (depending on the edge). Element maps were obtained by integrating over 60 eV after the edge for Mn and Ge.

Theoretically, the signal of ionization edge I_k can be quantified using standardless method, following the relation:

$$I_k = n_{\mathrm{den}} I \sigma_k \tag{1}$$

where n_{den} is the areal density (atom/nm^2) of a given element, I the total integrated number of counts in the spectrum and σ_k the cross section of ionization of an electron in the corresponding electron shell. Taking advantage of the high dynamical range of the spectra provided by the acquisition in dual-EELS mode, we can measure the total integrated number of counts I (Eq. 1) in the spectrum — from the intense zero-loss peak to the Ge and Mn edges.

In practice, the integration is performed over a finite energy range Δ and the collection angle β is limited by the entrance aperture of the spectrometer. These experi-

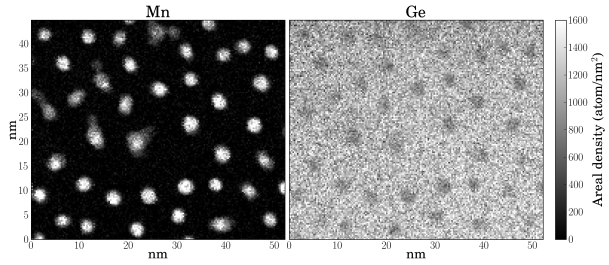

FIG. 2. Mn and Ge areal density maps obtained by EELS measurements.

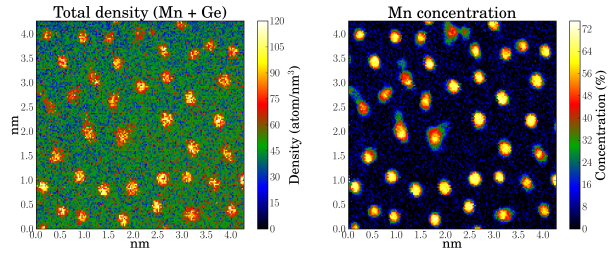

FIG. 3. Total density and Mn relative concentration maps obtained by EELS measurements.

mental parameters are taken into account in the calculation of the partial cross-sections, which depend on Δ, on the collection angle β and on the energy loss. For the Ge and Mn quantification we calculated parametrized partial Hartree-Slater cross sections[2] using the Gatan Digital Micrograph software.

By further measuring the specimen thickness, we can calculate the absolute volumic density (atom/nm^3) of each species.

To check the reliability of our analysis, we performed two cross checks:

- The experimental value for the Ge volumic density in the diamond Ge pure matrix is in good agreement — within 10 % — with the corresponding theoretical value (44 atoms/nm^3).

- The Mn concentration averaged over the whole concentration map is in good agreement — within 2% — with the Mn nominal concentration of the Ge(Mn) film measured with Rutherford backscattering spectrometry (RBS).

Figure 2 shows the Mn and Ge areal density maps obtained by the method explained previously. The total density (Mn + Ge density) is calculated by dividing the total areal density (Mn + Ge areal density) by the specimen thickness. Figure 3 shows the total density and the Mn relative concentration maps. Profiles measured on two nanocolumns are plotted in Fig. 4.

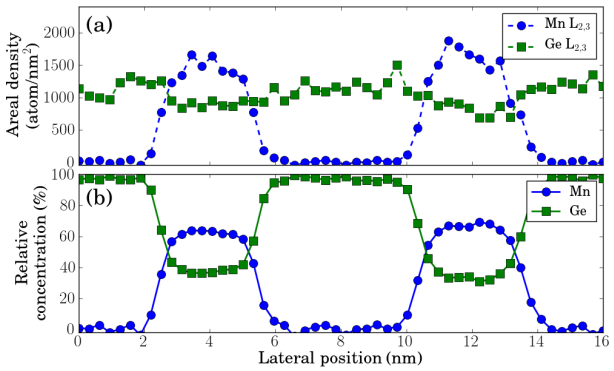

FIG. 4. (a) Areal density and (b) relative concentration profiles measured across two nanocolumns.

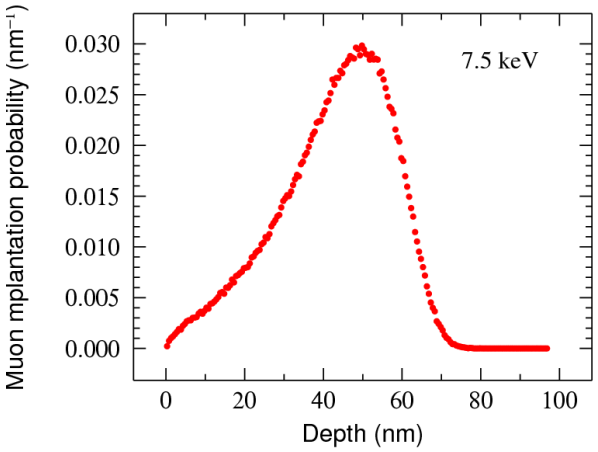

FIG. 5. Distribution of the depth implantation profile for muons of 7.5 keV kinetic energy. The simulation has been performed using the Monte Carlo code TRIM.SP (Refs. 3–5) code for a GeMn film with a Ge:Mn atomic ratio of 9:1.

II. MUON SPIN MEASUREMENTS

In Sec. II A we display the muon implantation profile computed for muons with 7.5 keV kinetic energy. Section II B provides additional information on the TF-μSR measurements. We finally describe the detailed analysis of the ZF-μSR data in Sec. II C.

A. Profile of muon implantation

Muons of 7.5 keV kinetic energy were used for the μSR measurements reported in the main text. From the implantation depth profile shown in Fig. 5, we can conclude that all the muons are implanted within the film thick-

ness of 80 nm.

B. Transverse field μSR

The TF-μSR spectrum displayed in Fig.4a of the main text exhibits two beating oscillating components. A first analysis for $100 \leq T \leq 200$ K indicates the amplitude of the more rapidly damped component to be temperature independent. Below 100 K the damping of this first component becomes quite large. As a consequence its initial amplitude, damping, precession frequency and initial phase are determined with limited precision. Fixing the initial amplitude allows a better accuracy on the other three parameters down to 40 K. To a good approximation, the precession frequency of the second component is constant in the whole temperature range with an average $\nu_2 = 1.353$ MHz. This corresponds to $B_{\rm ext}$, i.e. $\nu_2 = \nu_{\rm ext} = \gamma_\mu B_{\rm ext}/(2\pi)$. Here $\gamma_\mu = 851.6\ {\rm Mrad\,s^{-1}\,T^{-1}}$ is the muon gyromagnetic ratio. This discussion justifies the formula of Eq. 1 in the main text which is used to analyze the TF-μSR spectra.

C. Zero field μSR

From the two spectra recorded at 300 K, see Fig. 5 of the main text, we measure $a_0 \simeq 0.23$ (0.13) when $\mathbf{S}_\mu$ is parallel (perpendicular) to the film substrate. The smaller a_0 value for the perpendicular geometry follows from the geometrical setup of the spectrometer.

A qualitative discussion of the ZF-spectra is given in the main text. Here we quantitatively describe them. The measured asymmetry can be modelled consistently with the TF-μSR model[6]

$$a_0 P_{Z\,\parallel}^{\rm exp}(t) = \alpha \left\{ a_{\rm mat} \exp[-(\lambda_{Z\,\parallel\,{\rm mat}} t)^\beta] + a_{\rm c} \exp(-\lambda_{Z\,\parallel\,{\rm c}} t) + a_{\rm bg} \right\}, \qquad (2)$$

where $\lambda_{Z\,\parallel\,{\rm mat}}$ and $\lambda_{Z\,\parallel\,{\rm c}}$ are spin-lattice relaxation rates. The $\alpha = 1.05$ geometrical parameter is introduced to account for the slight difference in the signal amplitude between the TF and ZF geometries. Naturally we assign the first (second) term in Eq. 2 to muons stopped in the matrix (cores and their vicinity) while the last one concerns muons which have missed the sample. We find values for $a_{\rm mat}$, $a_{\rm c}$, and $a_{\rm bg}$ in line with the TF results. Fitting Eq. 2 to the data, we obtain $\lambda_{Z\,\parallel\,{\rm mat}}(T)$ (see Fig. 5c of the main text), $\lambda_{Z\,\perp\,{\rm c}}(T)$ and an exponent β equal to 0.6 between 200 and 50 K with a tendency to increase at lower temperature. At room temperature, $\beta = 1$ provides a good fit to the data.

Recalling the results obtained in TF measurements, and the structure of the film, one can deduce that the distance from muons concerned by the first component in Eq. 2 to the nearest Mn ions spans between 0.8 and 3 nm. This is a situation reminiscent of the dilute canonical spin glasses. In such systems, the polarization function has been derived in the case of fast fluctuating moments to be $P_Z(t) = \exp[-\sqrt{\lambda_Z t}]$,[7,8] a function which is close to our observation. The relaxation rate λ_Z is related to the magnetic fluctuation time τ of the Mn spins in the shell through the formula $\lambda_Z = 4\gamma_\mu^2 \Delta_{\rm L}^2 \tau$, where $\Delta_{\rm L}$ is the half-width at half-maximum of the component field Lorentzian distribution.[9]

Finally a few ZF spectra have been recorded after prior cooling of the film with $B_{\rm ext} = 150$ mT perpendicular to the film substrate. Within the data error bars no difference is found with the spectra measured after the usual ZFC procedure.

---

[1] Hyperspectral data analysis toolbox; see `http://hyperspy.org/`.

[2] R. Egerton, *Electron Energy-Loss Spectroscopy in the Electron Microscope* (Springer, 2011).

[3] W. Eckstein, *Computer Simulation of Ion-Solid Interactions* (Springer, Berlin, 1991).

[4] E. Morenzoni, T. Prokscha, A. Suter, H. Luetkens, and R. Khasanov, J. Phys.: Condens. Matter **16**, S4583 (2004).

[5] E. Morenzoni, H. Glückler, T. Prokscha, R. Khasanov, H. Luetkens, M. Birke, E. Forgan, C. Niedermayer, and M. Pleines, Nucl. Instr. and Meth. B **192**, 254 (2002).

[6] Given the similitude of the data recorded for the initial muon polarization perpendicular and parallel to the film and since a_0 is much larger for the latter geometry, we concentrate our discussion on it.

[7] Y. J. Uemura, T. Yamazaki, D. R. Harshman, M. Senba, and E. J. Ansaldo, Phys. Rev. B **31**, 546 (1985).

[8] A. Yaouanc and P. Dalmas de Réotier, *Muon Spin Rotation, Relaxation, and Resonance: Applications to Condensed Matter*, International Series of Monographs on Physiscs 147 (Oxford University Press, Oxford, 2011).

[9] R. E. Walstedt and L. R. Walker, Phys. Rev. B **9**, 4857 (1974).